GeroScience
https://doi.org/10.1007/s11357-026-02258-z

ORIGINAL ARTICLE

Autophagy revealed as a targetable vulnerability in senescent cells by cell painting phenotypic profiling: a mechanistic study of MCOPPB and related compounds

Matthew Lacey · Lucie Beresova · Alzbeta Srovnalova · Pavlo Polishchuk · Michal Sala · Zdenek Skrott · Marian Hajduch · Petr Dzubak · Jiri Bartek · Anna Siskova · Martin Loffelmann · Radim Nencka · Martin Mistrik

Received: 7 August 2025 / Accepted: 2 April 2026

Abstract Senescent cells accumulate with age and contribute to tissue dysfunction and chronic inflammation. Senolytic agents that selectively eliminate senescent cells hold therapeutic promise; however, few mechanistic classes have been established. Using Cell Painting–based morphological profiling, we identified a distinct cluster of senolytic compounds comprised of both known and novel autophagy inhibitors, including AZ191, bafilomycin A1, chloroquine, daurisoline, dauricine, MCOPPB, and its derivative MS1108. These compounds selectively eliminated senescent cells by disrupting autophagic flux. Our findings reveal senescent cell dependence on autophagy as an essential survival mechanism, define the existence of a mechanistically distinct class of senolytics acting through autophagy inhibition, and demonstrate the predictive value of Cell Painting in aging-related drug discovery. Our results provide new insights into senescent cell vulnerability and expand the therapeutic landscape for aging-related pathologies by highlighting autophagy as a targetable dependency.

Keywords Autophagy · Senescence · Senolytics · Cell Painting · SASP · Proteotoxic stress

Abbreviations

AISC	Autophagy inhibitor–senolytic cluster
BafA1	Bafilomycin A1
BJ	BJ foreskin fibroblasts
DAPI	4’,6-Diamidino-2-phenylindole
BSA	Bovine serum albumin
ER	Endoplasmic reticulum
FBS	Fetal bovine serum
N/OFQ	Nociceptin/orphanin FQ peptide (ligand)
NOP	Nociceptin/orphanin FQ (receptor)
PBS	Phosphate-buffered saline

Supplementary Information The online version contains supplementary material available at https://doi.org/10.1007/s11357-026-02258-z.

M. Lacey · L. Beresova · A. Srovnalova · P. Polishchuk · Z. Skrott · M. Hajduch · P. Dzubak · A. Siskova · M. Loffelmann · M. Mistrik (✉)
Institute of Molecular and Translational Medicine, Faculty of Medicine and Dentistry, Palacky University and University Hospital, Olomouc, Czech Republic
e-mail: martin.mistrik@upol.cz

M. Lacey · Z. Skrott · M. Hajduch · P. Dzubak · M. Mistrik
Institute of Molecular and Translational Medicine, Czech Advanced Technologies and Research Institute, Palacky University, 77147 Olomouc, Czech Republic

M. Sala · R. Nencka
Institute of Organic Chemistry and Biochemistry of the, Czech Academy of Science, CAS, Prague, Czech Republic

J. Bartek
Danish Cancer Institute, Danish Cancer Society, Copenhagen, Denmark

J. Bartek
Division of Genome Biology, Department of Medical Biochemistry and Biophysics, Science for Life Laboratory, Karolinska Institute, Stockholm, Sweden

Published online: 30 April 2026

RPE-1	HTERT-immortalized retinal pigment epithelial cells
SASP	Senescence-associated secretory phenotype
p62	SQSTM1
XTT	2,3-Bis(2-methoxy-4-nitro-5-sulfophenyl)-2H-tetrazolium-5-carboxanilide viability assay

Introduction

Cellular senescence is a durable form of cell cycle arrest [1, 2], induced by diverse stressors, including telomere dysfunction [3, 4], oncogenic signaling [5, 6], and DNA damage [3, 7]. While initially protective against tumorigenesis and essential during development and tissue repair, the chronic accumulation of senescent cells, typical for advanced ontological stages [8], contributes to tissue malfunction, inflammation, and organismal aging [8, 9]. Senescent cells are resistant to apoptosis and produce a pro-inflammatory senescence-associated secretory phenotype (SASP), which can propagate damage in a paracrine manner to surrounding tissues [1, 2, 5, 10–12].

Senolytics, compounds that selectively eliminate senescent cells, have shown considerable promise in preclinical models of delaying or partly reversing aging, or improving chronic conditions such as cancer therapy–induced tissue degeneration, fibrotic disorders, and metabolic diseases [10, 11, 13–16]. This has led to an intense interest in identifying novel senolytic compounds with clinical potential. Although several senolytics have been described, including inhibitors of BCL-2 family proteins [17], PI3K-AKT pathway modulators [18], HSP90 inhibitors [19], and others [20], the repertoire remains limited and the mechanistic understanding of senescent cell vulnerabilities is still evolving.

Autophagy, a lysosome-dependent catabolic system that degrades and recycles damaged proteins and organelles, plays a complex and context-dependent role in cellular senescence [21]. Autophagy can antagonize senescence by preserving mitochondrial and proteostatic integrity [22, 23], but paradoxically, many types of senescent cells exhibit increased autophagic flux that supports long-term survival and facilitates SASP production by both providing amino acids for the production of SASP factors and counteracting the endoplasmic reticulum (ER) and proteotoxic stress arising from SASP production [22, 24–26]. This has raised the hypothesis that senescent cells may be "autophagy-addicted," relying on sustained autophagic activity to maintain metabolic function and cope with chronic stress, including the proteotoxic stress caused by SASP production [22, 25, 27].

Notably, a few autophagy inhibitors, such as bafilomycin A1 (BafA1) [15] and chloroquine [28], have been sporadically reported to exert senolytic-like effects in vitro. Still, these observations remain underexplored and have not led to a widely accepted categorization of autophagy inhibitors as a distinct class of senolytics. The therapeutic potential of targeting autophagy in senescent cells thus remains largely untapped.

In a prior phenotypic screen for novel senolytics, we identified MCOPPB, a nociceptin/orphanin FQ peptide (NOP) receptor agonist [29], as a potent senolytic agent in vitro and in vivo [30]. Surprisingly, here we found that MCOPPB's senolytic activity is independent of NOP receptor signaling. To investigate its mechanism of action, we employed the Cell Painting assay, a multiplexed high-content imaging approach developed by the Broad Institute [31], which labels major cellular compartments and extracts high-dimensional morphological signatures, allowing systematic profiling of compound-induced phenotypes. Individual profiles are compared using dimensionality reduction (UMAP) and similarity-based clustering against a curated JUMP reference library that collects compounds with known mechanisms of action. This approach enables unbiased identification of compounds that induce phenotypically related cellular states. This approach revealed that MCOPPB clusters with multiple structurally diverse autophagy inhibitors. Functional validation experiments confirmed that MCOPPB indeed inhibits autophagy and that this inhibition is sufficient to induce selective death of senescent cells.

Overall, we identified a mechanistically coherent cluster of senolytic compounds that act by interfering with autophagic flux, thereby identifying autophagy as a targetable vulnerability of senescent cells. Our study also expands the mechanistic landscape of senolysis and contributes to the ongoing search for targeted senolytic therapies with translational potential.

Materials and methods

Chemicals

Compounds used in study include the following: aphidicolin (Sigma-Aldrich, A0781), BafA1 (MedChemExpress, HY-100558), chloroquine (Sigma-Aldrich, C6628), dauricine (PhytoLab, PHL80419), daurisoline (Sigma-Aldrich, SML0597), LY 2940094 (Med Chem Express, Hy114452), MCOPPB (Sigma-Aldrich, PZ0159), nociceptin ligand (Millipore, 487,960), and PP242 (MedChemExpress, HY-10474). MCOPPB derivatives (MS compounds) MS1108 and MS1109 were synthesized by the Institute of Organic Chemistry and Biochemistry of the CAS. See the Supplementary File and Fig. S1 for details. All molecular formulas were drawn with ChemDraw (version 19).

Cell culture

BJ foreskin fibroblasts (BJ), hTERT-immortalized retinal pigment epithelial cells (RPE-1), and HepG2 hepatocellular carcinoma cells were obtained from ATCC (ATCC numbers: CRL-2522, CRL-4000, and HB-8065, respectively). The BJ and RPE-1 cell lines were cultured in DMEM medium (Capricorn Scientific, DMEM-HPSTA [lot CP23-6033]) supplemented with 10% fetal bovine serum (FBS, Gibco, 10,270,106) and 1% penicillin/streptomycin (Sigma-Aldrich, P4333). Medium for BJ fibroblasts was further supplemented with non-essential amino acids (Gibco, 11,140,050) at 1% volume by volume. HepG2 cells were cultured in RPMI Medium 1640 with GlutaMAX™ (Gibco, 61,870–010), supplemented with 10% FBS Superior (Sigma-Aldrich, S0615). All cells were mycoplasma-free and cultured at 100% humidity and 37 °C with 5% CO_2.

Senescence induction

Cellular senescence was induced in BJ and RPE-1 cells using aphidicolin, as described previously [30]. Briefly, cells were cultivated in 150 cm^2 culturing flasks (TPP) for 7 weeks in media supplemented with 0.4 μM aphidicolin. Senescence induction started approximately on 5 million cells of either cell line (BJ or RPE-1) per flask. Every time the cells reached full confluency, they were trypsinized by TrypLE Express (Gibco, 12,605–028) and split equally from one flask into two. This process was repeated until a complete growth arrest. Control cells were cultured in parallel, without the addition of aphidicolin.

Senescence-associated-β-galactosidase staining

Senescence-associated β-Galactosidase Staining Kit (Cell Signaling Technology, 9860) was used to confirm the cellular senescence state following the aphidicolin treatment. Following the manufacturer's instructions, cells were seeded into six-well plates. Once settled, the medium was aspirated from the seeded cells (either senescent or proliferating), which were then washed with phosphate-buffered saline (PBS) (137 mM NaCl, 2.7 mM KCl, 4.3 mM Na_2HPO) before fixation with the fixative provided in the kit. Following fixation, cells were washed with PBS and incubated overnight at 37 °C, fully immersed in the pH-adjusted β-galactosidase staining solution (provided in the kit). Finally, the cells were examined and photographed using a transmission light microscope (Primo Vert, Zeiss, Oberkochen, Germany) equipped with a 4 × objective.

EdU incorporation–based cell proliferation assay

Cells were seeded into glass-bottom 96-well plates (Cellvis, P96-1.5H-N) at a density of 2000 senescent cells or 20,000 proliferating cells per well using BJ or RPE-1 cell lines. Proliferating cells were allowed to adhere for 24 h, whereas senescent cells were allowed to settle for 48 h prior to EdU incorporation. Cells were then incubated with 10 μM EdU for 48 h.

Following incubation, cells were washed with PBS, fixed in 4% paraformaldehyde (PFA) in PBS for 15 min at room temperature, and permeabilized with 0.5% (v/v) Triton X-100 in PBS (Sigma-Aldrich, T8787) for 3 min. EdU detection was performed using a click-chemistry reaction in staining solution containing 100 mM Tris (pH 8.5), 1 mM $CuSO_4$, 100 mM ascorbic acid, and 1 μM Alexa Fluor 488–azide (Invitrogen, A10266). Samples were incubated for 30 min at room temperature, protected from light. Cells were subsequently washed with PBS and counterstained with 1 μg/mL 4′,6-diamidino-2-phenylindole (DAPI; Thermo Fisher Scientific). Samples were then subjected to fluorescence microscopy.

For representative confocal images of nuclear EdU incorporation, samples were imaged using a confocal laser scanning microscope (LSM 980, Carl Zeiss) equipped with a Plan-Apochromat 20×/0.8 NA objective (Zeiss). DAPI and Alexa Fluor 488 were excited using 405 nm and 488 nm laser lines, respectively, with appropriate emission detection settings. Image acquisition was performed using ZEN software (blue edition, Zeiss), and identical acquisition parameters were maintained within each experimental series to ensure comparability.

For quantitative analysis of EdU signal per nucleus, images were acquired using an automated inverted fluorescence microscope (IX81, Olympus) equipped with a UPLSAPO 40×objective (Olympus) and filter sets for DAPI and FITC. Image acquisition was performed using ScanR Acquisition software (Olympus), and subsequent analysis was conducted with ScanR Analysis software (Olympus). Nuclei were segmented based on DAPI staining, and EdU positivity was determined by integrated signal intensity within the corresponding nuclear region in the EdU (FITC) channel.

Cell viability assay

Senescent cells were seeded in 24-well plates (TPP) at a density of 6000 cells per well and allowed to adhere and stabilize for 48 h prior to treatment. Proliferating cells were seeded in parallel at 100,000 cells per well and incubated for 24 h before treatment. Distinct seeding densities were empirically optimized to account for the pronounced differences in cell size and proliferative capacity between proliferating and senescent populations. The objective was to achieve comparable culture confluency at the time of treatment, with both conditions forming a confluent monolayer, thereby minimizing confounding effects arising from disparities in surface coverage and cell–cell contact [19, 32]. All cells were treated with four concentrations of the test compounds or mock-treated (more details are in the figure legends) for 24 h before assessment of viability. Viability was assessed using the 2,3-bis(2-methoxy-4-nitro-5-sulfophenyl)−2H-tetrazolium-5-carboxanilide viability assay (XTT, AppliChem, A8088) according to the instructions. Briefly, 150 µL of XTT solution made up of both the XTT activator and reagent was added to the cells in each well and incubated for 1–3 h, and absorbance at 475 nm was measured in a plate reader/spectrometer (Infinite® 200 Pro, TECAN, Männedorf, Switzerland).

Crystal violet assay

96-well plates (TPP) were used for crystal violet assays, with senescent cells seeded at 2000 cells per well and given 48 h to settle before treatment. In contrast, proliferating cells were seeded at 20,000 cells per well and given 24 h to settle before treatment. As with the XTT cell viability assays described above, distinct seeding densities were empirically optimized to account for the pronounced differences in cell size and proliferative capacity between proliferating and senescent populations. The objective was to achieve comparable culture confluency at the time of treatment, with both conditions forming a confluent monolayer, thereby minimizing confounding effects arising from disparities in surface coverage and cell–cell contact. According to the cell viability assay protocol (detailed above), all cells were treated with four concentrations of the test compounds or mock treatment and incubated for 24 h. Twenty-four hours after treatment, the medium was removed, and the cells were fixed using ice-cold 70% ethanol. They were then immediately stained with a 5% solution of crystal violet (Sigma-Aldrich C6158). Excess stain was washed off with water. The stained cells were air-dried. Once dry, contrast material (powdered white edible sugar) was added to each well, and the plates were scanned using a table scanner (Epson Perfection V750 PRO) to obtain representative images. For further quantification of the crystal violet signal, the contrast material was removed, and all the cell-incorporated crystal violet was dissolved using 5% acetic acid. The absorbance of the resulting solution was measured at 590 nm using a plate reader/spectrometer (Infinite® 200 Pro, TECAN, Männedorf, Switzerland).

Western blotting

For western blot analysis, 200,000 senescent cells, or 1,000,000 proliferating cells, were seeded into 60-mm tissue culture dishes in 5 mL of medium. Senescent cells were allowed to settle for 48 h before treatment; proliferating cells were allowed to settle for 24 h before treatment. Cells were seeded in this manner to match culture confluency between senescent and

proliferating cells at time of treatment. Lysates were prepared 24 h after treatment using Laemmli Sample Buffer (LSB, 50 mM Tris–HCl [pH 6.8]; 100 mM DTT; 2.0% SDS; 0.1% bromophenol blue; 10% glycerol).

SDS–polyacrylamide gel electrophoresis was carried out to separate 20 µg of protein per sample using 4–20% precast gels (Bio-Rad Laboratories, 4,561,096). Proteins were then transferred to a nitrocellulose membrane, and band sizes were determined using Precision Plus Protein Dual Color Standard (Bio-Rad Laboratories, 1,610,374). Membranes were cut to visualize several proteins of different molecular weights. Membrane blocking and antibody incubation were done using 5% milk in Tris-buffered saline (50 mM Tris–HCl, 150 mM NaCl [pH of 7.6]) with 0.1% Tween (MP Biomedicals, 103,168). Primary antibodies were incubated overnight at 4 °C, followed by washing in Tris-buffered saline and 1-h incubation with secondary antibodies at room temperature. Signal was visualized using a chemiluminescent substrate, a 3:1 mix of SuperSignal™ West Pico PLUS (Thermo Fisher Scientific, 34,580) and SuperSignal™ West Femto Maximum Sensitivity Substrate (Thermo Fisher Scientific, 34,095). Blot imaging was carried out using a BIORAD ChemiDoc MP imaging system (Bio-Rad Laboratories, CA, USA).

Mock treated samples were used for NOP receptor western blotting. For the purposes of examining autophagic flux, apart from the negative control (mock treated cells), another control sample was prepared—cells treated by a known autophagy activator PP242.

Primary antibodies included β-actin (1:1000; Santa Cruz Biotechnology, sc-47778), SMC1 (1:5000; Abcam, ab9262), SQSTM1/p62 (1:500; Cell Signaling, 88,588), LC3A/LC3B (1:1000; Invitrogen, PA1-16,931), and pS346-NOP (1:200; 7TM, 7TM0320A). Secondary antibodies included HRP-linked anti-mouse (1:1000; GE Health Care, NA931), and HRP-linked anti-rabbit (1:1000; GE Health Care, NA934).

Cell painting assay

HepG2 cells were counted using the ViCell cell counter (Beckman Coulter Inc., CA, USA) and then seeded into 384-well plates (PhenoPlate 384-well, Perkin Elmer, 6,057,328) with a Multidrop microplate dispenser (Thermo Fisher Scientific, MA, USA). A final volume of 40 µL per well was used, with 2000 cells per well. The plates were left at room temperature for 1 h to achieve homogeneous confluency. Afterward, the plates were incubated for 24 h at 37 °C in a 5% CO_2 atmosphere to allow cell attachment and propagation.

Compounds were transferred to the cell plates using an Echo 650 acoustic dispenser (Beckman Coulter, CA, USA), with transfer performed from low dead volume plates (Beckman Coulter, CA, USA). After compound addition, the plates were incubated for 24 h at 37 °C in a 5% CO_2 atmosphere.

The Cell Painting staining protocol follows the original published methodology of Bray et al. [31] with slight modifications according to Wolff et al. [33]. Briefly, the medium was aspirated from the plates, leaving a residual volume of 10 µl. Next, 30 µl of a MitoTracker (Invitrogen, M22426) solution in pre-warmed medium (RPMI without phenol red) was added to the cells, resulting in a final concentration of 500 nM. The cells were incubated for 30 min at 37 °C. The MitoTracker solution was removed and replaced with 30 µl of 4% paraformaldehyde (EMS, 15,714-1L), and the plates were incubated in the dark at room temperature for 20 min. After fixation, the cells were washed with 70 µl PBS and then permeabilized by adding 30 µl of a 0.1% (v/v) Triton X-100/PBS (Sigma-Aldrich, T8787) and incubated for 20 min at room temperature. Triton X-100 solution was removed, and the cells were washed twice with 70 µl PBS. Next, the staining solution, containing HOECHST 33342 (Invitrogen, H3570), SYTO14 green (Invitrogen, S7576), concanavalin A/Alexa Fluor 488 (Invitrogen, C11252), wheat germ agglutinin/Alexa Fluor 555 (Invitrogen, W32464), and phalloidin/Alexa Fluor 568 (Invitrogen, A12380) in PBS with 1% (m/v) Bovine Serum Albumin (Sigma-Aldrich, A7030), was added to the wells (30 µl per well). The final concentrations in each well were as follows: 4 µM HOECHST, 25 µg/ml concanavalin A, 3 µM SYTO14, 1 U/ml phalloidin, and 1.5 µg/ml wheat germ agglutinin. The cells were stained in the dark at room temperature for 30 min. After staining, the cells were washed three times with 70 µl PBS. The plates were then sealed with adhesive foil and stored in the dark at 4 °C until image acquisition. The devices used in the fixation, staining, and washing processes included BioTek EL406 (BioTek Instruments, Inc., USA) for aspiration and dispensing,

Certus Flex (Fritz Gyger AG) for dispensing, and Blue Washer (BlueCatBio, Germany) for washing.

Stained fixed cells were acquired using an automated confocal microscope, Yokogawa CV8000, with a water-immersion 20×objective (1.0 NA). For each well of the 384-well plate, nine fields arranged in a 3×3 grid at the well's center were captured. Imaging was performed across four fluorescence channels to detect HOECHST 33342 (Ex, 405 nm; Em, 400–490 nm), concanavalin A and SYTO14 (Ex, 488 nm; Em, 500–550 nm), and wheat germ agglutinin and phalloidin (Ex, 561 nm; Em, 563–637 nm), as well as MitoTracker (Ex, 640 nm; Em, 647–705 nm).

Signals Image Artist (SImA1.3) from Revvity (Hamburg, Germany) was used for image data analysis. The analysis involved the following channels: Alexa488, Alexa568, Mitotracker647, and Hoechst33342. In each input image, the cell populations were defined by "Find Nuclei" (Hoechst33342), and "Find Cytoplasm" (Alexa488) instructions. Then, the perinuclear region and cellular membrane region were selected. The texture (SER Features, Gabor Features, and Haralick Features), intensity, and morphology properties (area, roundness, width, length, ratio width to length, and advanced morphology properties [using the STAR method]) were calculated in all four channels in all predefined regions, yielding over 500 different features.

Properties were extracted per cell, and the mean and the standard deviation per well were used for further processing. The total number of features per well was 1065. Feature processing was conducted utilizing Pycytominer (version 1.1.0) according to the published protocol [34]. Briefly, feature values for individual plates underwent normalization through the "mad_robustize" method. The normalized values were calculated as the difference between a specific feature value and the median value of dimethyl sulfoxide (AppliChem)–treated wells on the respective plate, divided by the median absolute deviation of the dimethyl sulfoxide–treated well values, with an addition of 10–18 to ensure that the denominator does not equal zero. Subsequently, feature selection was executed by eliminating features that contained missing values, those exhibiting low variance (with frequency and uniqueness cutoffs set at 0.1), highly correlated features (correlation coefficient exceeding 0.9), and features with extreme values (outlier cutoff set at 100). Finally, median feature values were determined across all wells associated with the same compound at identical concentrations. Using in-house scripts, the analysis of median profiles of compounds, the construction of UMAP [35], and visualization were carried out in R (version 4.4.0). UMAPs were built using median values of selected features for individual compounds at a given concentration.

For our reference set of compounds, we utilized the JUMP dataset [36], which comprises 306 compounds selected according to specific criteria: (i) the compounds must target proteins encoded by genes from diverse gene families; (ii) at least two compounds should target each gene product; and (iii) each compound should ideally target only a single gene product; however, achieving this last criterion proved challenging due to the complexities associated with polypharmacology.

Immunofluorescence microscopy

Cells were seeded into glass-bottom 96-well plates (Cellvis, P96-1.5H-N) at a density of 2000 senescent cells or 20,000 proliferating cells per well, using either BJ or RPE-1 cell lines. Proliferating cells were allowed to adhere for 24 h, whereas senescent cells were allowed to settle for 48 h prior to treatment. Cells were then treated with the indicated test compounds or vehicle control and incubated for 24 h (compound concentrations are specified in the respective figure legends).

Following treatment, cells were washed with PBS, fixed in 4% paraformaldehyde (PFA) in PBS for 15 min at room temperature, and permeabilized with 0.5% (v/v) Triton X-100 in PBS (Sigma-Aldrich, T8787) for 3 min. Non-specific binding was blocked with 1% bovine serum albumin (BSA; Sigma-Aldrich, A9647) in PBS for 30 min at room temperature. Samples were incubated overnight at 4 °C with primary antibody against SQSTM1/p62 (1:500; Cell Signaling Technology, #88,588), followed by washes in 1% BSA/PBS and incubation with Alexa Fluor 488-conjugated anti-mouse secondary antibody (1:1000; Invitrogen, A-11001) for 1 h at room temperature. Nuclei were counterstained with DAPI (1 µg/mL in water) for 10 min. After final PBS washes, samples were air-dried and imaged by fluorescence microscopy.

Immunofluorescence-stained samples were imaged using a confocal laser scanning microscope (LSM 980, Carl Zeiss). A C-Apochromat 40×/1.2 NA

water-immersion objective (Zeiss) was employed for all acquisitions. Fluorophores were excited using 405-nm and 488-nm lasers for DAPI and Alexa Fluor 488, respectively, with corresponding emission filter settings. Image acquisition was performed using ZEN software (blue edition, Zeiss) under identical settings within each experimental series to ensure comparability.

Statistical analysis

XTT analysis and crystal violet readings are displayed as percentage viability compared to mock treated samples, with results normalized to mock treated cells in Microsoft Excel (version 2504). GraphPad Prism 10.4.2 for Windows (GraphPad Software, Boston, MA, USA) was used to calculate the means and ± standard deviations; in all cases, three independent biological repeats were carried out. Each biological replicate for XTT senolytic viability screenings consisted of four technical replicates, while crystal violet assays consisted of three technical replicates.

HepG2 viability following treatments in the Cell Painting assay were determined by comparing the number of objects in treated wells, compared to the number of objects in DMSO-treated control wells. Mean number of objects and ± standard deviations from four replicates were calculated in Microsoft Excel (version 2504). For results, see Supplementary Table 1.

XTT and crystal violet data for senolytic screening was plotted as an XY line graph with each point representing a calculated mean and error bars illustrating the ± standard deviations. Graphs were created using GraphPad Prism 10.4.2 for Windows (GraphPad Software, Boston, MA, USA).

The percentage of EdU-positive nuclei among total nuclei was calculated from two biological repeats for each tested cell line and is shown as the mean + SD.

Results

Senescence induction and validation

In this work, we utilized two commonly used human cell lines: the diploid strain of BJ foreskin fibroblasts (BJ) and the hTERT-immortalized retinal pigment epithelial cells (RPE-1); the latter incapable of replicative senescence due to telomere attrition yet still undergoing other types of senescence when exposed to appropriate insults. In both models, we induced cellular senescence via prolonged treatment with 0.4 μM aphidicolin, a well-established inducer of replication stress in vitro, when applied at low doses [37]. Aphidicolin is a particularly efficient inducer of cellular senescence [30, 38], likely due to the formation of replication stress-induced chromosomal breakage within the chromosomal common fragile sites, leading to persistent DNA damage [39, 40]. Successful induction of cellular senescence was validated using multiple complementary criteria. Senescence-associated β-galactosidase (SA-β-Gal) activity was confirmed by histochemical staining (Fig. 1c, f). Senescent cells further exhibited the characteristic enlarged and flattened morphology (see microscopic images in Fig. 1c and f and Fig. 5). In addition, proliferative arrest was verified by a 48-h incubation with EdU, a thymidine analogue incorporated into newly synthesized DNA during S phase, visualized and quantified by fluorescence microscopy. While proliferating cells show high EdU nuclear positivity (81% ± 15% for BJ cells, 95% ± 3.5% for RPE-1 cells) in senescence counterpart, there was almost no detectable EdU incorporation (nuclear EdU positivity1.3% ± 0.1% for BJ cells, 1.9% ± 0.9% for RPE-1 cells) (Fig. S2).

Senolytic activity of MCOPPB was independent of nociceptin signaling

We compared the senolytic effects of MCOPPB and two newly synthesized structural derivatives of MCOPPB, termed MS1108 and MS1109, which differ by minor chemical modifications (Fig. 1a), with those of nociceptin/orphanin FQ peptide (N/OFQ). This 17-amino acid neuropeptide is the endogenous ligand for the NOP receptor. Senolytic activity was assessed in two cellular models of pharmacologically induced senescence as detailed above. Surprisingly, despite all of the tested compounds activating NOP receptor to a similar extent, as assessed by phosphorylation on Serine 346 (Fig. 1d, g) [41], only MCOPPB and its derivative MS1108 exhibited preferential toxicity toward senescent cells (Fig. 1b, e), suggesting a NOP-independent senolytic mechanism.

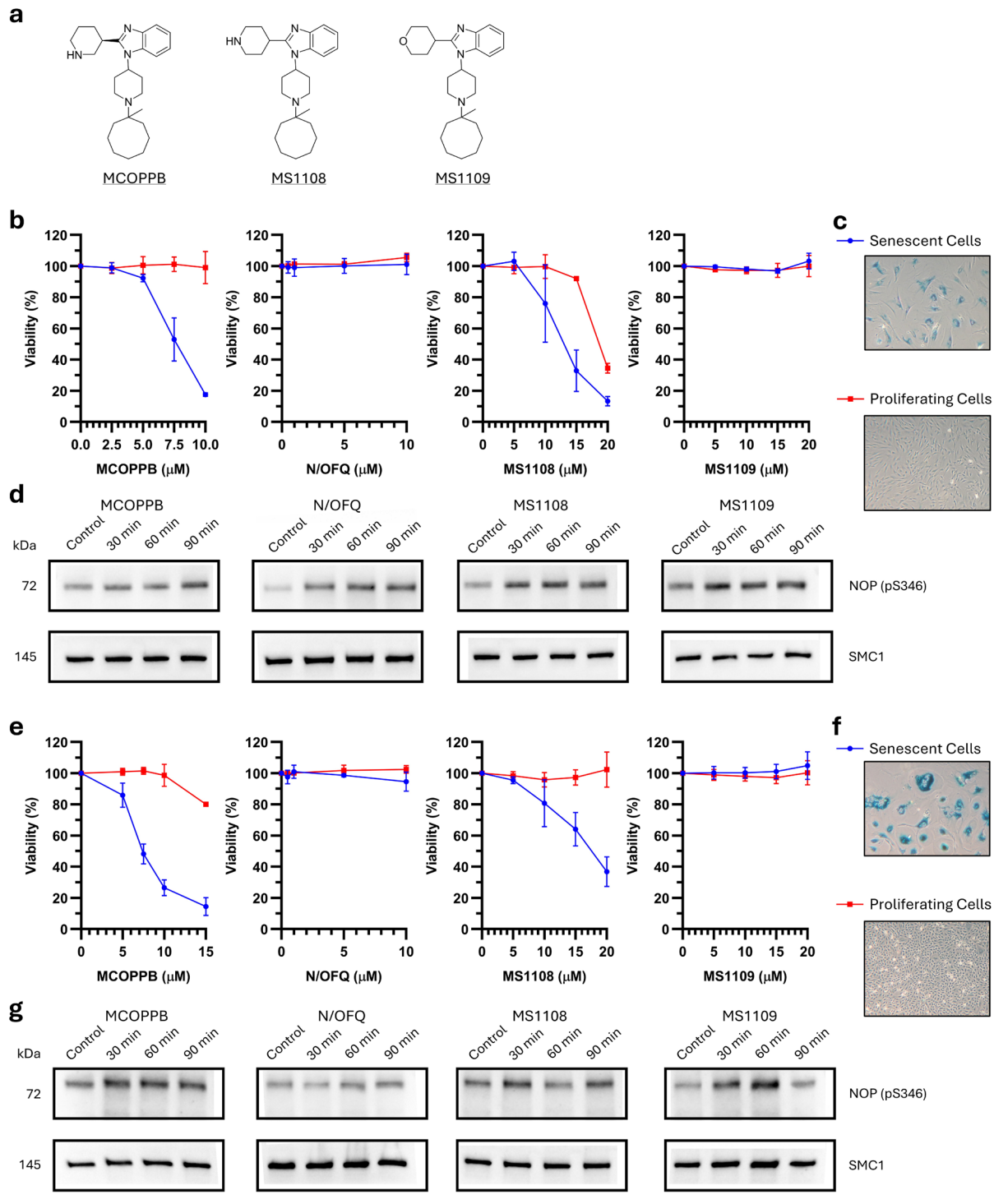
a
MCOPPB
MS1108
MS1109
b
Viability (%)
MCOPPB (μM)
N/OFQ (μM)
MS1108 (μM)
MS1109 (μM)
c
Senescent Cells
Proliferating Cells
d
MCOPPB
N/OFQ
MS1108
MS1109
Control
30 min
60 min
90 min
kDa
72
145
NOP (pS346)
SMC1
e
f
g

◂**Fig. 1** Senolytic activity is NOP receptor signaling independent. **a** Chemical structures of MCCOPB and its two derivatives, MS1108 and MS1109. **b** Results of viability assays (XTT) where proliferating (red lines) and senescent (blue lines) BJ fibroblasts were exposed to increasing concentrations of MCOPPB (2.5, 5, 7.5, and 10 μM), N/OFQ (0.5, 1, 5, and 10 μM), MS1108 (5, 10, 15, and 20 μM), and MS1109 (5, 10, 15, and 20 μM) for 24 h. **c** Microphotographs of the proliferating and senescent BJ fibroblasts used in the experiment after Senescence Associated-β-Gal staining (40× magnification). **d** Western blot analysis of NOP receptor activation (NOP [pS346]) for the tested compounds (all treatments were 10 μM) in BJ fibroblasts in mock treated cells and post treatment at 30, 60, and 90 min; SMC1 shown as loading control. Western blot images compiled from different blots. **e** Results of Viability assays (XTT) where proliferating (red lines) and senescent (blue lines) RPE-1 retinal cells were exposed to increasing concentrations of MCOPPB (5, 7.5, 10, and 15 μM), N/OFQ (0.5, 1, 5, and 10 μM), MS1108 (5, 10, 15, and 20 μM), and MS1109 (5, 10, 15, and 20 μM) for 24 h. **f** Microphotographs of the proliferating and senescent RPE-1 retinal cells used in the experiment after Senescence Associated-β-Gal staining (40× magnification). **g** Western blot analysis of NOP receptor activation (NOP [pS346]) for the tested compounds (all treatments were 10 μM) in RPE-1 cells in mock treated cells and post-treatment at 30, 60, and 90 min; SMC1 shown as loading control. Western blot images compiled from strips taken from a single membrane

Autophagy inhibition as a candidate off-target mechanism of MCOPPB and MS1108

As the identification of off-targets is often challenging, we next turned to Cell Painting. This method was developed by the Broad Institute [31], and is based on a multiplexed high-content imaging approach that labels major cellular compartments and extracts high-dimensional morphological signatures, allowing systematic profiling of compound-induced cellular phenotypes. Our implementation includes compound treatment and staining of HepG2 cells with six fluorescent labels including Hoechst 33,342 (nuclei), MitoTracker (mitochondria), concanavalin A (endoplasmic reticulum), phalloidin (actin cytoskeleton), SYTO14 (nucleoli/cytoplasmic RNA), and wheat germ agglutinin (plasma membrane/glycoproteins) (Fig. S3). Automated confocal imaging followed by segmentation of nuclei and cytoplasm enabled extraction of > 1000 morphological, intensity, and texture features per well. After normalization and feature selection, median compound profiles were compared using dimensionality reduction (UMAP) and similarity-based clustering against a curated JUMP reference library, which gathers compounds of known mechanism of action, including off-target effects [33]. This approach allows unbiased identification of compounds inducing phenotypically related cellular states, including effects of the compounds on viability (Supplementary Table 1).

We profiled MCOPPB and its two derivatives, alongside known senolytics (ABT263, quercetin, fisetin, and dasatinib) [20], and included daurisoline, a related hit from our previous senolytic screen [30], and its structural analog dauricine. Clustering based on morphological features revealed that MCOPPB and its senolytically active derivative MS1108 did not co-cluster with any of the established senolytics but instead formed a relatively distinct cluster with daurisoline and dauricine (Fig. 2), compounds chemically unrelated to MCOPPB. Interestingly, both daurisoline and dauricine are known natural inhibitors of autophagy [42], suggesting that autophagy disruption may be a potential shared mechanism revealed by the Cell Painting clustering. To explore this possibility further, we expanded the profiling across a range of concentrations and included two canonical autophagy inhibitors, chloroquine [43] and BafA1 [44]. Strikingly, BafA1, chloroquine, dauricine, daurisoline, MCOPPB, and MS1108 converged in the same distinct morphological cluster (Fig. 3a, b), reinforcing the idea that interference with autophagy may underlie the senolytic activity. Notably, AZ191, a DYRK1B inhibitor from the JUMP reference library, also co-clustered within this group despite not being previously known as an autophagy inhibitor.

Autophagy inhibitors co-clustering with MCOPPB exhibited senolytic activity

Further functional validation via XTT assay confirmed that all members of the aforementioned cluster, including AZ191, induced cell death preferentially in senescent BJ and RPE-1 cells (Fig. 4a, b). A complementary cell toxicity assay (to avoid possible XTT assay bias) was performed using direct staining of surviving cells via a crystal violet assay (Fig. S4). Additionally, Western blot analysis of senescent cells treated with the same set of compounds revealed the accumulation of LC3-II and SQSTM1 (p62), established markers of autophagic flux inhibition [45] (Fig. 4c). Therefore, the identified cluster of compounds can be described as the Autophagy Inhibitor Senolytic Compound (AISC) Cluster. In contrast,

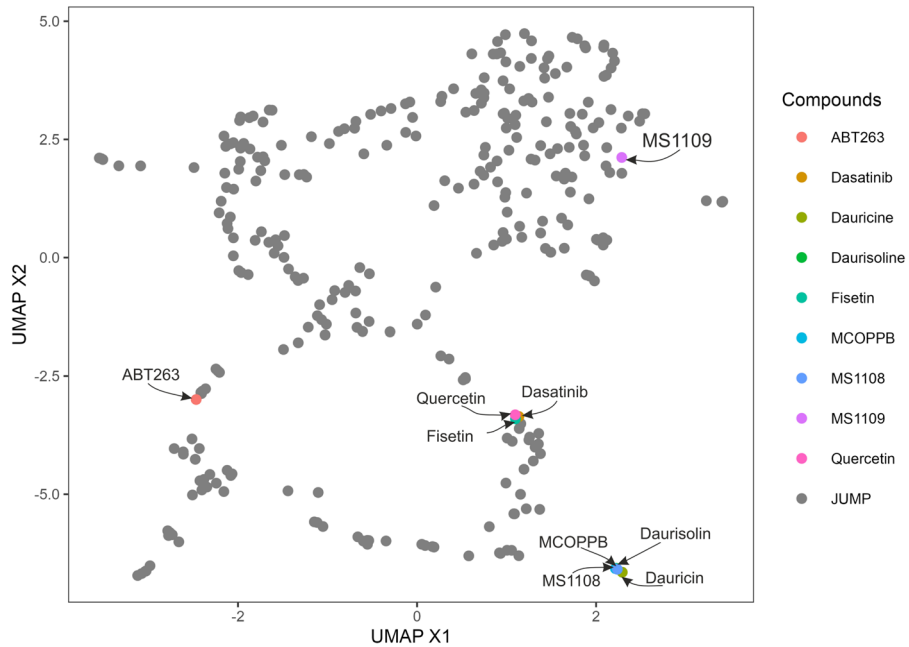

Fig. 2 Morphological profiling of effects of MCOPPB and its derivatives using the Cell Painting assay. Clustering analysis of the initial Cell Painting assay involving MCOPPB and its two derivatives (MS1108 and MS1109), daurisoline (a compound identified in our initial senolytic screen), its structural analog dauricine, and established senolytics ABT263, quercetin, fisetin, and dasatinib. All compounds were tested at 10 µM, except dasatinib (1 µM). Phenotypic profiles were compared to the JUMP library (grey dots) using clustering based on image-derived features. MCOPPB, MS1108, daurisoline, and dauricine form a visible distinct cluster. MS1109, MCOPPB derivative with nociceptin agonist but not senolytic activity, stays aside this cluster (purple dot)

MS1109, which lacked both senolytic activity and cluster membership, did not affect these markers, serving as a negative control (Fig. S5).

To further delineate autophagy status and to assess the impact of the newly identified autophagy inhibitors, we compared the effects of MCOPPB, MS1108, and AZ191 on autophagic flux in proliferating and senescent cells. All three compounds inhibited autophagic flux in both cellular states. However, direct quantitative comparison by Western blotting is intrinsically complicated by the pronounced hypertrophy of senescent cells, which can occupy the surface area equivalent of several proliferating cells (see microscopic images in Fig. 1c and f, and Fig. 5). Consequently, total protein input does not directly reflect cell number, and protein abundance cannot be interpreted on a per-cell basis.

To standardize loading conditions, lysates were in this case normalized for total protein. Under this loading, senescent cells exhibited generally lower p62 response and approximately comparable LC3-I and LC3-II response relative to proliferating cells. Notably, the signal of SMC1, used here as a nuclear-associated loading control, was substantially reduced in senescent samples, consistent with a lower number of nuclei (and therefore fewer cells) contributing to the same total protein input (Fig. S6).

To overcome the intrinsic limitations of Western blot–based comparisons, we complemented our analysis with quantitative immunofluorescence of p62 in proliferating and senescent cells across both cellular models following treatment with the newly identified compounds and established autophagy inhibitors. In all cases, treatment resulted in a clear increase in p62 signal relative to mock-treated controls, consistent with impaired autophagic degradation. Notably, compound-specific differences in p62 accumulation were observed between proliferating and senescent states, as well as between the two cellular models, underscoring context-dependent effects on autophagic flux (Fig. 5).

Overall, these results indicate that autophagy interference may be the shared mechanism underlying the senolytic activity of the newly identified senolytics.

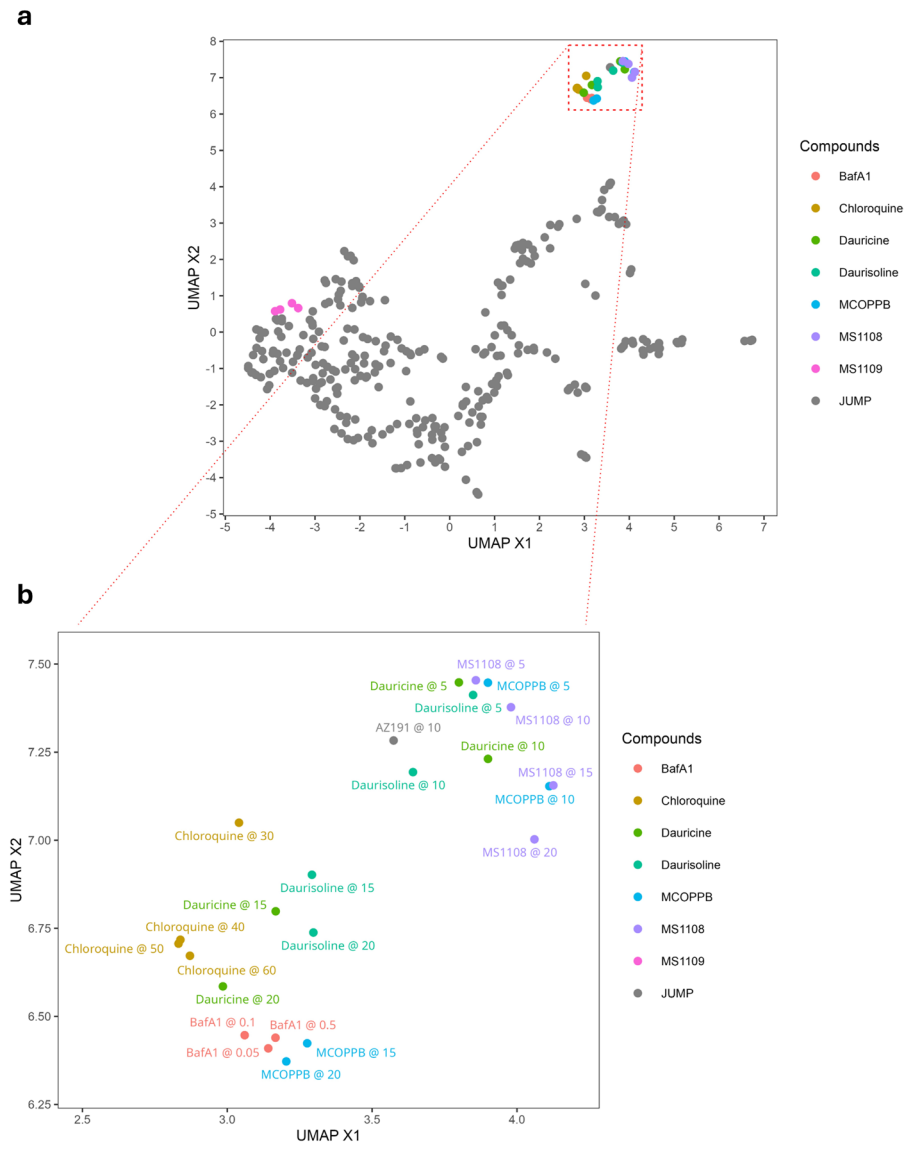

Fig. 3 Concentration-expanded morphological profiling with added canonical autophagy inhibitors. Cells were treated with MCOPPB, MS1109, MS1108, and known autophagy inhibitors chloroquine, BafA1, daurisoline, and dauricine at various concentrations and assessed using the phenotypic profiling method (Cell Painting assay), in which compound-induced morphological changes are compared with reference compounds of known molecular targets (JUMP library). **a** Cluster analysis of morphology-derived features revealed a separate cluster of known autophagy inhibitors (chloroquine, BafA1, daurisoline, and dauricine) which also included MCOPPB and MS1108. MS1109, MCOPPB's derivative with nociceptin agonist but not senolytic activity, stays aside from this cluster (pink dots). **b** The detailed zoom of the cluster with highlighted individual compounds and the concentrations used in μM. Note that AZ191, a compound from the JUMP reference library, also co-clustered within this cluster

Discussion

While several senolytic compounds have entered early-phase clinical trials [46], the need for new senolytic agents remains high due to cell-type specificity [32, 47] and pharmacokinetic challenges. For example, quercetin, despite strong preclinical data, fails to penetrate the cerebrospinal fluid, limiting its utility in neurodegenerative contexts [48]. In this study, we demonstrated that the Cell Painting assay, initially designed for mechanism-of-action prediction, can be effectively repurposed to identify novel senolytics by exploiting cellular morphological similarities observed following treatment with either known, mechanistically characterized compounds or selected test compounds, offering a scalable and unbiased high-content approach to mechanistic profiling. Through the extraction of hundreds of morphological features, including subtle morphological changes, from images and then comparing them across annotated reference libraries, Cell Painting enables the discovery of shared mechanisms, including off-target effects, that would otherwise require extensive biochemical, genetic, and computational analyses.

In this study, we employed Cell Painting and identified a mechanistically coherent cluster of senolytic

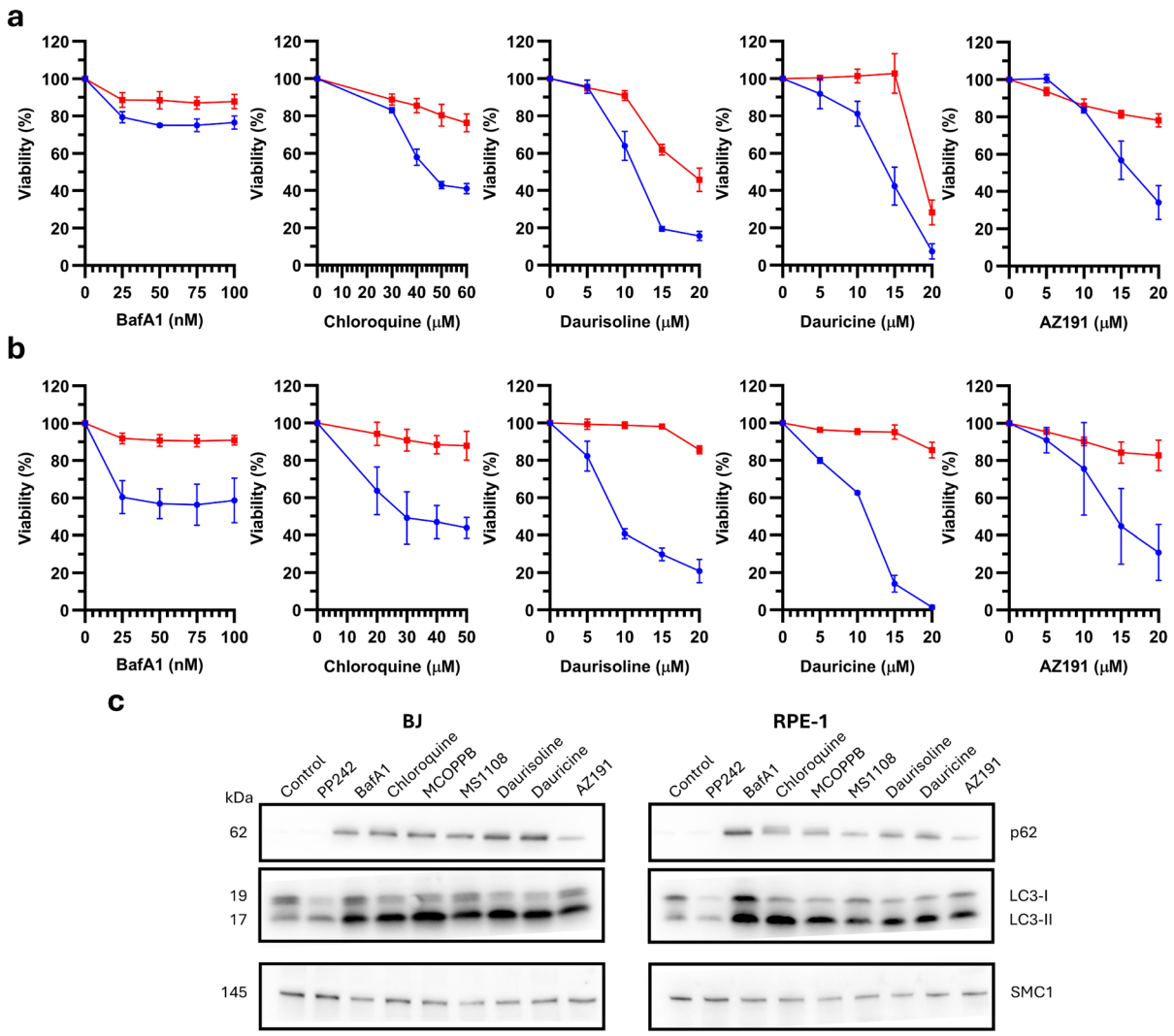

Fig. 4 Senolytic and autophagy-inhibitory effects of compounds co-clustering in the Cell Painting assay with MCOPPB and MS1108. **a** Viability assessment (XTT) of proliferating (red lines) and senescent (blue lines) BJ fibroblasts after exposure to increasing concentrations of the compounds for 24 h (BafA1 [25, 50, 75, and 100 nM]; chloroquine [30, 40, 50, and 60 μM]; daurisoline [5, 10, 15, and 20 μM]; dauricine [5, 10, 15, and 20 μM]; AZ191 [5, 10, 15, and 20 μM]). **b** Viability assessment (XTT)of proliferating (red lines) and senescent (blue lines) RPE-1 retinal cells after exposure to increasing concentrations of the compounds for 24 h (BafA1 [25, 50, 75, and 100 nM]; chloroquine [20, 30, 40, and 50 μM]; daurisoline [5, 10, 15, and 20 μM]; dauricine [5, 10, 15, and 20 μM]; AZ191 [5, 10, 15, and 20 μM]). **c** Western blots illustrating the effects of the compounds on autophagy inhibition in senescent cells, as assessed by elevated p62 and LC3-II proteins. SMC1 is shown as a loading control. Elevated p62 and LC3-II compared to control (Ctrl) were observed in BafA1, chloroquine, MCOPPB, MS1108, daurisoline, and dauricine treatments. Compound PP242 is a known autophagy activator and was used as a control. Treatment concentrations: PP242 (1 μM), BafA1 (50 nM), chloroquine (40 μM), MCOPPB (BJ: 7.5 μM, RPE-1: 10 μM), MS1108 (10 μM), daurisoline (10 μM), dauricine (10 μM), AZ191 (BJ: 15 μM, RPE-1: 20 μM). Western blot images compiled from strips taken from a single membrane

compounds, as illustrated in Fig. 2 and Fig. 3. The reproducible co-clustering of our compounds with canonical autophagy inhibitors within the Cell Painting reference space suggested functional convergence on autophagy-related processes. It is important to emphasize that Cell Painting does not directly quantify autophagic flux; rather, it captures high-dimensional morphological signatures reflecting the

integrated cellular consequences of pathway perturbation, including organelle redistribution, altered cytoplasmic granularity, and mitochondrial remodeling. In this context, the assay proved highly informative as an unbiased systems-level phenotyping platform.

Nevertheless, several limitations must be acknowledged. First, Cell Painting does not identify primary molecular targets. The profiles reflect downstream phenotypic states rather than direct target engagement. Accordingly, phenotypic convergence should be interpreted as functional similarity at the systemic level. Compounds acting on distinct molecular nodes within a shared biological process, such as lysosomal acidification, autophagosome-lysosome fusion, or broader proteostasis regulation, may produce highly correlated morphological signatures despite targeting different proteins. In addition, although the JUMP reference library is extensively curated, strict target selectivity is uncommon, and polypharmacology remains prevalent. Thus, clustering with annotated compounds may indicate shared pathway perturbation, partially overlapping off-target effects, or both. Finally, dimensionality reduction approaches such as UMAP emphasize preservation of local neighborhood structure and can influence the apparent geometry of clusters in two-dimensional space.

For these reasons, phenotypic similarity derived from Cell Painting should be regarded as hypothesis-generating rather than definitive. Consistent with this principle, the clustering-based hypothesis implicating autophagy inhibition was subsequently tested using subsequent biochemical assays, which confirmed impaired autophagic flux. Using Western blotting and immunofluorescence analyses of established autophagic flux markers, we demonstrated that MCOPPB and its derivative MS1108 inhibit autophagy. This effect is independent of their known activity as nociceptin/orphanin FQ peptide (NOP) receptor agonists. We further established that autophagic flux inhibition and the associated senolytic activity of these compounds are not mediated through NOP receptor signaling. Pharmacological activation of the NOP receptor alone did not recapitulate the effects on autophagy or cell viability, indicating that the observed phenotype arises from an off-target mechanism unrelated to canonical NOP receptor engagement.

Furthermore, we identified three new senolytic compounds, daurisoline, dauricine, and MS1108 (a derivative of MCOPPB), and independently corroborated the previously reported senolytic activity of AZ191 [49]. Notably, all four compounds co-clustered in the Cell Painting reference space within a group enriched for established autophagy inhibitors, which we designated the Autophagy Inhibitor–Senolytic Cluster (AISC). Importantly, each compound within the AISC not only impaired autophagic flux but also exhibited preferential cytotoxicity toward senescent cells, albeit to varying degrees, indicating a shared mechanistic axis coupled with quantitative differences in senolytic potency.

Preferential toxicity toward senescent cells does not exclude measurable cytotoxicity in proliferating populations. In our experiments, higher concentrations of MS1108, daurisoline, and dauricine produced evident toxicity in proliferating BJ cells. Such cell line–dependent effects are not unprecedented; similar observations have been reported for established senolytics, including dasatinib, quercetin, and ABT263 (navitoclax) [32, 47]. Heterogeneity in senolytic efficacy across cellular contexts is likewise well documented. For example, we observed that senescent RPE-1 cells were more sensitive to chloroquine than senescent BJ fibroblasts (see Fig. 4 and Fig. S4). Comparable cell type–specific differences have been described for other senolytics [32, 47, 50]. Such variability likely reflects mechanistic differences at the level of autophagy regulation and lysosomal biology, as distinct compounds interfere with discrete nodes of the autophagic pathway. For instance, both BafA1 and chloroquine impair lysosomal acidification, but through mechanistically distinct routes. BafA1 inhibits the vacuolar H^+-ATPase (V-ATPase), thereby preventing proton translocation into lysosomes and blocking acidification [44], a mechanism considered central to its autophagy-inhibitory activity [51]. In contrast, chloroquine accumulates within lysosomes and acts as a weak base to neutralize luminal pH [52]. In addition, both compounds have been reported to interfere with autophagosome–lysosome fusion, a mechanism thought to substantially contribute to chloroquine-mediated autophagy inhibition [43, 44].

Off-target activities may further modulate cell type–specific responses and overall senolytic potency. Analogous to chloroquine, daurisoline and dauricine have been reported to inhibit autophagosome–lysosome fusion [42, 43]. Nevertheless, we observed quantitative differences in senolytic efficacy among these compounds (see Figs. 1, 4, and S4), suggesting

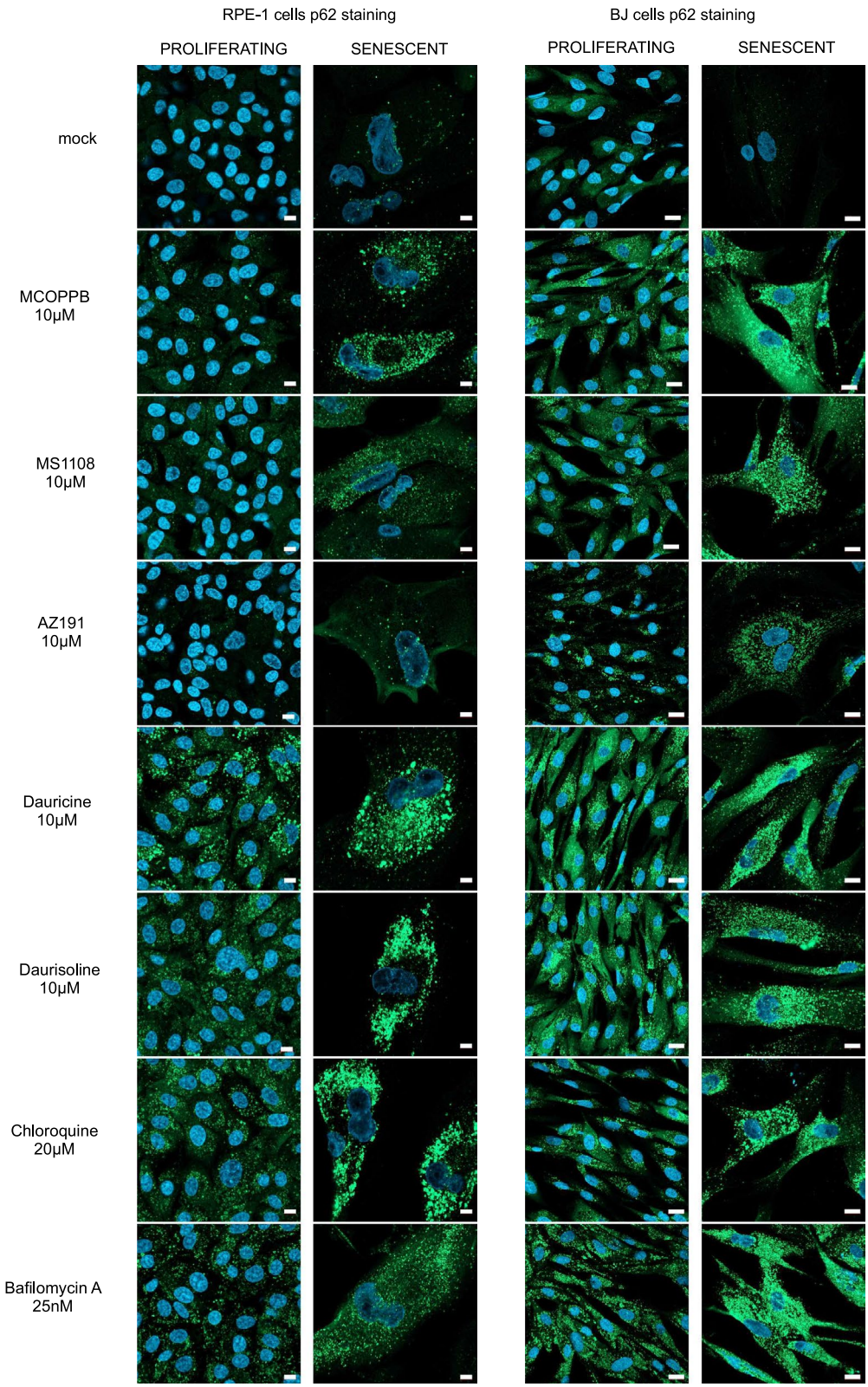
RPE-1 cells p62 staining
BJ cells p62 staining
PROLIFERATING
SENESCENT
PROLIFERATING
SENESCENT
mock
MCOPPB 10μM
MS1108 10μM
AZ191 10μM
Dauricine 10μM
Daurisoline 10μM
Chloroquine 20μM
Bafilomycin A 25nM

◂**Fig. 5** Immunofluorescence analysis of p62 foci in proliferating and senescent cells following treatment with AISC compounds. Proliferating and senescent BJ and RPE-1 cells were treated for 24 h with either vehicle (mock) or the indicated AISC compounds. Treatment concentrations were as follows: MCOPPB (10 μM), MS1108 (10 μM), AZ191 (10 μM), daurisoline (10 μM), dauricine (10 μM), chloroquine (20 μM), and bafilomycin A1 (25 nM). Accumulation of p62/SQSTM1 was assessed by immunofluorescence microscopy. Treatment with AISC compounds led to an increase in the number of p62-positive foci in both proliferating and senescent cells across both cell lines. Notably, p62 accumulation was markedly more pronounced in senescent cells, consistent with their increased susceptibility to autophagy inhibition relative to proliferating counterparts. (Scale bars: 10 μm for RPE-1 cells and 20 μm for BJ cells)

that additional molecular determinants influence cellular susceptibility. Such variation may ultimately be advantageous, as it raises the possibility of tailoring senolytic strategies to specific tissues or pathological contexts based on their underlying autophagy dependencies.

Autophagy (specifically macroautophagy) is known to decline with advancing age [8]; as a result, targeting autophagy for senolysis may appear to be counterintuitive. However, macroautophagy has been expressly proven to be upregulated in senescent cells [26], where it facilitates the production of the SASP within senescent cells by supplying amino acids via the TOR-autophagy spatial coupling compartment [26, 53]. Furthermore, autophagy is known to mitigate the proteotoxic and ER stress inherent to SASP production; thus, it can be deduced that it functions as a pro-survival pathway in senescent cells [22, 26, 54]. Therefore, despite the overall decline of autophagy at an organismal level, senescent cells that accumulate with aging seems to be heavily dependent on the autophagy machinery.

The upregulation of macroautophagy in senescent cells [26] appears to be consistent with our own comparative analyses. Specifically, normalization of p62 and LC3 levels to SMC1, used as a nuclear-associated loading marker, or to the number of cells, would indicate higher macroautophagic activity in senescent relative to proliferating cells on a per-cell basis (Fig. S6). Pharmacological inhibition of autophagy has been shown to selectively eliminate senescent cells, also previously, by exacerbating ER stress and inducing cell death in SASP-positive populations [15]. ER stress–associated vulnerability may therefore mechanistically underlie the preferential sensitivity of senescent cells to autophagy inhibition observed in our models. Collectively, the senolytic activity observed for multiple compounds in our study that interfere with autophagic flux strongly supports a pro-survival role of autophagy, particularly macroautophagy, in senescent cells.

Our previous in vivo study describing the senolytic activity of MCOPPB [30] provides additional support for this model. In that work, MCOPPB administration led to a significant reduction in established markers of cellular senescence in hepatic tissue, consistent with senolytic efficacy in vivo. Unexpectedly, however, we also observed increased hepatic lipid accumulation. This finding was initially counterintuitive, as clearance of senescent cells has in some contexts been associated with reduced liver adiposity [55]. At the time, we attributed the phenotype to a modest increase in body weight and reduced locomotor activity following MCOPPB treatment, potentially related to its known anxiolytic properties.

In light of the present data, and considering the extensive literature underscoring the central role of macroautophagy in hepatic lipid turnover and lipophagy [56–58], inhibition of autophagic flux by MCOPPB offers a mechanistically coherent explanation for the observed lipid accumulation despite concurrent senolytic activity. Impaired autophagic degradation of lipid droplets would be expected to promote hepatic steatosis, even in the setting of reduced senescent cell burden. Thus, our current findings support the interpretation that MCOPPB functions as an autophagy inhibitor in vivo and suggest that the hepatic phenotype previously observed in treated mice may reflect systemic disruption of autophagic pathways rather than solely behavioral or metabolic secondary effects.

Conclusion

Together, our present findings have identified a new group of senolytic compounds, which includes MCOPPB and its derivative MS1108, that act by disrupting autophagic flux and demonstrate the dependence of senescent cells on functional autophagy, identifying autophagy as a previously underexploited vulnerability in senescent cells. Our work identified daurisoline, dauricine, and MS1108 as novel senolytics, and corroborated previously noted senolytic activity in AZ191, BafA1, and chloroquine.

Moreover, we show morphological profiling to be a valuable tool for detecting off-target effects, leading to mechanistic discoveries, such as the previously unappreciated senolytic mechanism revealed by the present study.

We propose a two-tiered screening strategy whereby morphological profiling is first used to identify candidate autophagy inhibitors, followed by secondary screening for senolytic activity. This approach is resource-efficient compared to broad phenotypic screens and offers a rational path for the discovery of novel senolytic compounds.

Author contribution MLa, MM, and JB conceived the study. MLa and MM designed most of the cellular experiments, which were performed mainly by MLa, ZS, and LB; cell toxicity assays were performed by MLa and MLo. The Cell Painting assay was designed and carried out by ASr, PP, PD, ASi, and MH. MS and RN synthesized the MCOPPB derivatives (MS1108 and MS1109), and AS and PP made the statistical analyses. MM, MLa, MH, and JB interpreted the results and wrote the manuscript, which was approved by all authors.

Funding Open access publishing supported by the institutions participating in the CzechELib Transformative Agreement. This work was supported by infrastructural projects (CZ-OPENSCREEN–LM2023052; EATRIS-CZ–LM2023053; Czech-BioImaging–LM2023050), and the project National Institute for Cancer Research (Program EXCELES, ID Project No. LX22NPO5102), funded by the European Union-Next Generation EU from the Ministry of Education, Youth and Sports of the Czech Republic (MEYS), SALVAGE project (Z.02.01.01/00/22_008/0004644), supported by OP JAK, with co-financing from the EU and the State Budget, by the Palacky University Olomouc Young Researcher Grant (JG_2023_33), by the project New Technologies for Translational Research in Pharmaceutical Sciences (NETPHARM, project ID CZ.02.01.01/00/22_008/0004607), co-funded by the European Union. This work was also supported by the Danish Cancer Society (R322-A17482), the Czech Academy of Sciences (RVO: 61388963), and an integral grant of Palacky University in Olomouc (IGA-UP-2021).

Data availability The datasets used and/or analyzed during the current study are available from the corresponding author on reasonable request.

Declarations

Conflict of interest The authors declare no competing interests.

References

1. Rodier F, Campisi J. Four faces of cellular senescence. J Cell Biol. 2011;192:547–56.
2. Gorgoulis V, Adams PD, Alimonti A, Bennett DC, Bischof O, Bishop C, et al. Cellular senescence: defining a path forward. Cell. 2019;179:813–27.
3. Rossiello F, Herbig U, Longhese MP, Fumagalli M, d'Adda di Fagagna F. Irreparable telomeric DNA damage and persistent DDR signalling as a shared causative mechanism of cellular senescence and ageing. Curr Opin Genet Dev. 2014;26:89–95.
4. de Magalhães JP, Passos JF. Stress, cell senescence and organismal ageing. Mech Ageing Dev. 2018;170:2–9.
5. Liu X-L, Ding J, Meng L-H. Oncogene-induced senescence: a double edged sword in cancer. Acta Pharmacol Sin. 2018;39:1553–8.
6. Bartkova J, Rezaei N, Liontos M, Karakaidos P, Kletsas D, Issaeva N, Vassiliou L-VF, Kolettas E, Niforou K, Zoumpourlis VC, Takaoka M, Nakagawa H, Tort F, et al. Oncogene-induced senescence is part of the tumorigenesis barrier imposed by DNA damage checkpoints. Nature. 2006;444: 633–7.
7. Bartek J, Bartkova J, Lukas J. DNA damage signalling guards against activated oncogenes and tumour progression. Oncogene. 2007;26:7773–9.
8. López-Otín C, Blasco MA, Partridge L, Serrano M, Kroemer G. Hallmarks of aging: an expanding universe. Cell. 2023;186:243–78.
9. He S, Sharpless NE. Senescence in health and disease. Cell. 2017;169:1000–11.
10. McHugh D, Gil J. Senescence and aging: causes, consequences, and therapeutic avenues. J Cell Biol. 2018;217:65–77.
11. Childs BG, Gluscevic M, Baker DJ, Laberge R-M, Marquess D, Dananberg J, et al. Senescent cells: an emerging target for diseases of ageing. Nat Rev Drug Discov. 2017;16:718–35.
12. Coppé J-P, Desprez P-Y, Krtolica A, Campisi J. The senescence-associated secretory phenotype: the dark side of tumor suppression. Annu Rev Pathol. 2010;5:99–118.
13. Gonzales MM, Garbarino VR, Marques Zilli E, Petersen RC, Kirkland JL, Tchkonia T, et al. Senolytic therapy to modulate the progression of Alzheimer's disease (SToMP-AD): a pilot clinical trial. J Prev Alzheimers Dis. 2022;9:22–9.

14. Xu M, Pirtskhalava T, Farr JN, Weigand BM, Palmer AK, Weivoda MM, et al. Senolytics improve physical function and increase lifespan in old age. Nat Med. 2018;24:1246–56.
15. Dörr JR, Yu Y, Milanovic M, Beuster G, Zasada C, Däbritz JHM, et al. Synthetic lethal metabolic targeting of cellular senescence in cancer therapy. Nature. 2013;501:421–5.
16. Baker DJ, Wijshake T, Tchkonia T, LeBrasseur NK, Childs BG, van de Sluis B, et al. Clearance of p16Ink4a-positive senescent cells delays ageing-associated disorders. Nature. 2011;479:232–6.
17. Chang J, Wang Y, Shao L, Laberge R-M, Demaria M, Campisi J, et al. Clearance of senescent cells by ABT263 rejuvenates aged hematopoietic stem cells in mice. Nat Med. 2016;22:78–83.
18. Fan Z, Tong Y, Yang Z, Wang S, Huang T, Yang D, et al. Inhibitor PF-04691502 works as a senolytic to regulate cellular senescence. Exp Gerontol. 2024;186:112359.
19. Fuhrmann-Stroissnigg H, Ling YY, Zhao J, McGowan SJ, Zhu Y, Brooks RW, et al. Identification of HSP90 inhibitors as a novel class of senolytics. Nat Commun. 2017;8:422.
20. Kirkland JL, Tchkonia T. Senolytic drugs: from discovery to translation. J Intern Med. 2020;288:518–36.
21. Li Q, Lin Y, Liang G, Xiao N, Zhang H, Yang X, et al. Autophagy and senescence: the molecular mechanisms and implications in liver diseases. Int J Mol Sci. 2023;24:16880.
22. Lee Y, Kim J, Kim M-S, Kwon Y, Shin S, Yi H, et al. Coordinate regulation of the senescent state by selective autophagy. Dev Cell. 2021;56:1512-1525.e7.
23. Choi I, Wang M, Yoo S, Xu P, Seegobin SP, Li X, et al. Autophagy enables microglia to engage amyloid plaques and prevents microglial senescence. Nat Cell Biol. 2023;25:963–74.
24. Cayo A, Segovia R, Venturini W, Moore-Carrasco R, Valenzuela C, Brown N. mTOR activity and autophagy in senescent cells, a complex partnership. Int J Mol Sci. 2021;22:8149.
25. Kim J, Lee Y, Jeon T, Kim M-S, Kang C. All cells are created equal in the sight of autophagy: selective autophagy maintains homeostasis in senescent cells. Autophagy. 2021;17:3260–1.
26. Kwon Y, Kim JW, Jeoung JA, Kim M-S, Kang C. Autophagy is pro-senescence when seen in close-up, but anti-senescence in long-shot. Mol Cells. 2017;40:607–12.
27. Deschênes-Simard X, Lessard F, Gaumont-Leclerc M-F, Bardeesy N, Ferbeyre G. Cellular senescence and protein degradation: breaking down cancer. Cell Cycle. 2014;13:1840–58.
28. L'Hôte V, Courbeyrette R, Pinna G, Cintrat J, Le Pavec G, Delaunay-Moisan A, et al. Ouabain and chloroquine trigger senolysis of BRAF-V600E-induced senescent cells by targeting autophagy. Aging Cell. 2021;20:e13447.
29. Hayashi S, Hirao A, Imai A, Nakamura H, Murata Y, Ohashi K, et al. Novel non-peptide nociceptin/orphanin FQ receptor agonist, 1-[1-(1-methylcyclooctyl)-4-piperidinyl]-2-[(3R)-3-piperidinyl]-1H-benzimidazole: design, synthesis, and structure-activity relationship of oral receptor occupancy in the brain for orally potent antianxiety drug. J Med Chem. 2009;52:610–25.
30. Raffaele M, Kovacovicova K, Biagini T, Lo Re O, Frohlich J, Giallongo S, et al. Nociceptin/orphanin FQ opioid receptor (NOP) selective ligand MCOPPB links anxiolytic and senolytic effects. Geroscience. 2022;44:463–83.
31. Bray M-A, Singh S, Han H, Davis CT, Borgeson B, Hartland C, et al. Cell painting, a high-content image-based assay for morphological profiling using multiplexed fluorescent dyes. Nat Protoc. 2016;11:1757–74.
32. Zhu Y, Tchkonia T, Pirtskhalava T, Gower AC, Ding H, Giorgadze N, et al. The Achilles' heel of senescent cells: from transcriptome to senolytic drugs. Aging Cell. 2015;14:644–58.
33. Wolff C, Neuenschwander M, Beese CJ, Sitani D, Ramos MC, Srovnalova A, et al. Morphological profiling data resource enables prediction of chemical compound properties. iScience. 2025;28:112445.
34. Serrano E, Chandrasekaran SN, Bunten D, Brewer KI, Tomkinson J, Kern R, Bornholdt M, Fleming S, Pei R, Arevalo J, Tsang H, Rubinetti V, Tromans-Coia C, et al. Reproducible image-based profiling with Pycytominer. ArXiv. 2024; : arXiv:2311.13417v2.
35. McInnes L, Healy J, Saul N, Großberger L. UMAP: uniform manifold approximation and projection. J Open Source Softw. 2018;3:861.
36. Chandrasekaran SN, Cimini BA, Goodale A, Miller L, Kost-Alimova M, Jamali N, et al. Three million images and morphological profiles of cells treated with matched chemical and genetic perturbations. Nat Methods. 2024;21:1114–21.
37. Vesela E, Chroma K, Turi Z, Mistrik M. Common chemical inductors of replication stress: focus on cell-based studies. Biomolecules. 2017;7:19.
38. Marusyk A, Wheeler LJ, Mathews CK, DeGregori J. p53 mediates senescence-like arrest induced by chronic replicational stress. Mol Cell Biol. 2007;27:5336–51.
39. Beresova L, Vesela E, Chamrad I, Voller J, Yamada M, Furst T, et al. Role of DNA repair factor xeroderma pigmentosum protein group C in response to replication stress as revealed by DNA fragile site affinity chromatography and quantitative proteomics. J Proteome Res. 2016;15:4505–17.
40. Lezaja A, Panagopoulos A, Wen Y, Carvalho E, Imhof R, Altmeyer M. RPA shields inherited DNA lesions for post-mitotic DNA synthesis. Nat Commun. 2021;12:3827.
41. Mann A, Moulédous L, Froment C, O'Neill PR, Dasgupta P, Günther T, et al. Agonist-selective NOP receptor phosphorylation correlates *in vitro* and *in vivo* and reveals differential post-activation signaling by chemically diverse agonists. Sci Signal. 2019;12:eaau8072.
42. Wu M-Y, Wang S-F, Cai C-Z, Tan J-Q, Li M, Lu J-J, et al. Natural autophagy blockers, dauricine (DAC) and daurisoline (DAS), sensitize cancer cells to camptothecin-induced toxicity. Oncotarget. 2017;8:77673–84.
43. Mauthe M, Orhon I, Rocchi C, Zhou X, Luhr M, Hijlkema K-J, et al. Chloroquine inhibits autophagic flux by decreasing autophagosome-lysosome fusion. Autophagy. 2018;14:1435–55.

44. Mauvezin C, Neufeld TP. Bafilomycin A1 disrupts autophagic flux by inhibiting both V-ATPase-dependent acidification and Ca-P60A/SERCA-dependent autophagosome-lysosome fusion. Autophagy. 2015;11:1437–8.
45. Zhou J, Tan S-H, Nicolas V, Bauvy C, Yang N-D, Zhang J, et al. Activation of lysosomal function in the course of autophagy via mTORC1 suppression and autophagosome-lysosome fusion. Cell Res. 2013;23:508–23.
46. Chaib S, Tchkonia T, Kirkland JL. Cellular senescence and senolytics: the path to the clinic. Nat Med. 2022;28:1556–68.
47. Zhu Y, Tchkonia T, Fuhrmann-Stroissnigg H, Dai HM, Ling YY, Stout MB, et al. Identification of a novel senolytic agent, navitoclax, targeting the Bcl-2 family of anti-apoptotic factors. Aging Cell. 2016;15:428–35.
48. Gonzales MM, Garbarino VR, Kautz TF, Palavicini JP, Lopez-Cruzan M, Dehkordi SK, et al. Senolytic therapy in mild Alzheimer's disease: a phase 1 feasibility trial. Nat Med. 2023;29:2481–8.
49. Pramotton FM, Abukar A, Hudson C, Dunbar J, Potterton A, Tonnicchia S, et al. DYRK1B inhibition exerts senolytic effects on endothelial cells and rescues endothelial dysfunctions. Mech Ageing Dev. 2023;213:111836.
50. Zhu Y, Doornebal EJ, Pirtskhalava T, Giorgadze N, Wentworth M, Fuhrmann-Stroissnigg H, et al. New agents that target senescent cells: the flavone, fisetin, and the BCL-XL inhibitors, A1331852 and A1155463. Aging Albany NY. 2017;9:955–63.
51. Klionsky DJ, Elazar Z, Seglen PO, Rubinsztein DC. Does bafilomycin A1 block the fusion of autophagosomes with lysosomes? Autophagy. 2008;4:849–50.
52. Gallagher LE, Radhi OA, Abdullah MO, McCluskey AG, Boyd M, Chan EYW. Lysosomotropism depends on glucose: a chloroquine resistance mechanism. Cell Death Dis. 2017;8:e3014.
53. Narita M, Young ARJ, Arakawa S, Samarajiwa SA, Nakashima T, Yoshida S, Hong S, Berry LS, Reichelt S, Ferreira M, Tavaré S, Inoki K, Shimizu S, et al. Spatial coupling of mTOR and autophagy augments secretory phenotypes. Science. New York, N.Y.; 2011; 332: 966–70.
54. Ogata M, Hino S, Saito A, Morikawa K, Kondo S, Kanemoto S, et al. Autophagy is activated for cell survival after endoplasmic reticulum stress. Mol Cell Biol. 2006;26:9220–31.
55. Ogrodnik M, Miwa S, Tchkonia T, Tiniakos D, Wilson CL, Lahat A, et al. Cellular senescence drives age-dependent hepatic steatosis. Nat Commun. 2017;8:15691.
56. Singh R, Kaushik S, Wang Y, Xiang Y, Novak I, Komatsu M, et al. Autophagy regulates lipid metabolism. Nature. 2009;458:1131–5.
57. Martinez-Lopez N, Singh R. Autophagy and lipid droplets in the liver. Annu Rev Nutr. 2015;35:215–37.
58. Stankov MV, Panayotova-Dimitrova D, Leverkus M, Vondran FWR, Bauerfeind R, Binz A, et al. Autophagy inhibition due to thymidine analogues as novel mechanism leading to hepatocyte dysfunction and lipid accumulation. AIDS. 2012;26:1995–2006.